UC San Diego
UC San Diego Previously Published Works

Title

ARN25068, a versatile starting point towards triple GSK-3β/FYN/DYRK1A inhibitors to tackle tau-related neurological disorders

Permalink

Authors

Demuro, Stefania
Sauvey, Conall
Tripathi, Shailesh K
et al.

Publication Date

DOI

Peer reviewed

ARN25068, a versatile starting point towards triple GSK-3β/FYN/DYRK1A inhibitors to tackle tau-related neurological disorders

Stefania Demuro[1,4], **Conall Sauvey**[2], **Shailesh K. Tripathi**[1], **Rita M. C. Di Martino**[1], **Da Shi**[2], **Jose A. Ortega**[1], **Debora Russo**[3], **Beatrice Balboni**[1,4], **Barbara Giabbai**[5], **Paola Storici**[5], **Stefania Girotto**[1], **Ruben Abagyan**[2,*], **Andrea Cavalli**[1,4,*]

[1]Computational and Chemical Biology, Istituto Italiano di Tecnologia, via Morego 30, 16163 Genoa, Italy.

[2]Skaggs School of Pharmacy and Pharmaceutical Sciences, University of California, San Diego, La Jolla, California 92093, United States.

[3]D3 PharmaChemistry, Istituto Italiano di Tecnologia, via Morego, 30, 16163 Genoa, Italy.

[4]Department of Pharmacy and Biotechnology, University of Bologna, Via Belmeloro 6, 40126 Bologna, Italy.

[5]Protein Facility, Elettra Sincrotrone Trieste S.C.p.A., SS 14 - km 163,5 in AREA Science Park, 34149, Trieste, Italy.

Abstract

The human kinome plays a crucial role in several pathways. Its dysregulation has been linked to diverse central nervous system (CNS)-related disorders with a drastic impact on the aging population. Among them, tauopathies, such as Alzheimer's Disease (AD) and Frontotemporal Lobar degeneration (FTLD-tau), are neurodegenerative disorders pathologically defined by the presence of hyperphosphorylated tau-positive intracellular inclusions known as neurofibrillary tangles (NFTs). Compelling evidence has reported the great potential of the simultaneous modulation of multiple protein kinases (PKs) involved in abnormal tau phosphorylation through a concerted pharmacological approach to achieve a superior therapeutic effect relative to classic "one target, one drug" approaches.

Here, we report on the identification and characterization of **ARN25068** (**4**), a low nanomolar and well-balanced dual GSK-3β and FYN inhibitor, which also shows inhibitory activity against

DYRK1A, an emerging target in AD and tauopathies. Computational and X-Ray studies highlight compound **4**'s typical H-bonding pattern of ATP-competitive inhibitors at the binding sites of all three PKs. In a tau phosphorylation assay on Tau0N4R-TM-tGFP U2OS cell line, **4** reduces the extent of tau phosphorylation, promoting tau-stabilized microtubule bundles. In conclusion, this compound emerges as a promising prototype for further SAR explorations to develop potent and well-balanced triple GSK-3β/FYN/DYRK1A inhibitors to tackle tau hyperphosphorylation.

Graphical Abstract
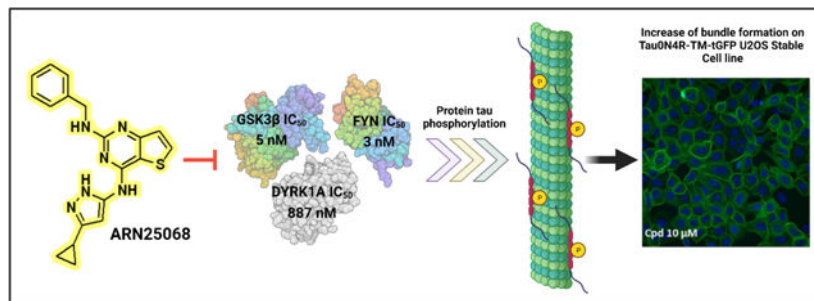
Keywords

central nervous system; tauopathies; kinase inhibitors; multitarget compounds; docking studies; X-ray studies; enzymatic and cell-based assays; tau phosphorylation assay; selectivity

INTRODUCTION

The protein kinases (PKs) represent increasingly attractive targets for central nervous system (CNS) drug discovery. The human kinome, composed of 518 different PKs [1], offers a wide range of new CNS-disease-relevant targets due to the master regulatory role of these enzymes in a myriad of signal transduction cascades [2]. PKs orchestrate multiple physiological processes by phosphorylation of specific serine (Ser), threonine (Thr) or tyrosine (Tyr) residues as part of signal- or condition-dependent post-translational modification events [3].

Dysregulation of these enzymes has been linked to a large portion of complex and multifactorial CNS-related disorders, including tauopathies, a class of neurodegenerative diseases such as Alzheimer's disease (AD) and frontotemporal lobar degeneration (FTLD-tau), which are pathologically defined by the presence of hyperphosphorylated tau-positive intracellular aggregates called neurofibrillary tangles (NFTs).

Tau is a microtubule (MT)-associated protein, expressed particularly in the axons of neurons with the primary function to promote MT stabilization. Under normal physiological conditions, this protein contributes to cellular and axonal stability by regulating trafficking and vesicle transport [4]. In neurons affected by tauopathies, abnormal phosphorylation of tau reduces its affinity for the MTs leading to tau detachment from the MTs then misfolding, and aggregation [5, 6].

The strong correlation between tau hyperphosphorylation and tauopathies has focused attention on tau kinases as validated targets in this field [7]. Among them, glycogen synthase kinase-3β (GSK-3β) proved to play a significant role in regulating tau phosphorylation, mainly at Ser199, Ser396, and Ser413, [8–11] under both physiological and pathological conditions. GSK-3β is a multitasking and ubiquitous 47-kDa Ser/Thr kinase highly expressed in the hippocampus, cerebral cortex, and the Purkinje cells of the cerebellum and involved in the phosphorylation of more than a hundred different substrates [12]. Dysregulation of this enzyme is believed to contribute to both onset and progression of various chronic conditions, including diabetes, cancer, neurodegenerative and behavioral diseases [13, 14].

FYN is a 59-kDa non-receptor Tyr kinase (TK) of Src family kinases (SFKs), [15] recently recognized as key mediator of amyloid-β (Aβ)/tau10-induced toxicity in AD, [16–18] physically linked to the *N*-terminal projection domain of tau and mediating phosphorylation of the latter at Tyr18 [19]. Alongside GSK-3β, this enzyme is present in many brain areas. It is involved in both development and adult brain physiology, modulating various cellular processes, including morphogenetic transformation and cell growth [20].

Over the last few years, intensive preclinical activity including both GSK-3β and FYN inhibitors has taken place; however, developing safe, brain-penetrant, and specific PKs inhibitors is highly challenging [21]. Furthermore, since *in vivo* tau-hyperphosphorylation results from multiple kinase activities, a single effective strategy to reverse tauopathies remains an open question [6]. Recently, ever-increasing interest has been directed to the concurrent modulation of multiple PKs involved in abnormal tau phosphorylation as a successful multitarget strategy for achieving a therapeutic effect [22].

As such, considering the crucial role of GSK-3β and FYN in tau phosphorylation, as well as the promise of multikinase inhibitors with specific beneficial profile designed to boost efficacy and overcome some limitations of single-target treatments [23, 24], we discovered the well-balanced dual GSK-3β/FYN inhibitor **ARN25068** (**4**) (Fig. 1) among a large set of compounds tested against 172 different PKs [25], for its chemical feasibility and low promiscuity as promising and versatile starting point for further investigations.

RESULTS AND DISCUSSION

In the present work, we report an in-depth evaluation of the binding properties of compound **4**, bearing a 2,4-di-substituted pyrimidine thiophene core, as a promising multikinase inhibitor with specific beneficial target profile able to reduce tau hyperphosphorylation in an *in vitro* model of AD.

First, docking simulations were performed to predict the bound conformations of **4** at both GSK-3β and FYN ATP binding pockets (Fig. 1). Flexible receptor models were generated for both proteins, and **4** was docked using the latest version of ICM pro software. Desirable docking scores of −39.3 and −39.5 were observed against GSK-3β and FYN, respectively. The binding poses of **4** in each receptor model resembled those of typical type I or II inhibitors, with hydrophobic and H-bond contacts between the compound and key

residues in the ATP binding sites of both enzymes (Fig. 1) [26]. When binding to GSK-3β, compound **4** was predicted to form 3 total H-bonds between its aminopyrazole core and residues V135 and D133 in the hinge region (Fig. 1A and 1B). Hydrophobic contacts were predicted between the pyrimidine core moiety of **4** and residues I62, T138, R141, E137, and P136, between the aminopyrazole core heterocycle and residues Y134, L188, and A83, between the cyclopropyl group and residues L132 and C199, and between the benzylamine moiety and residues V70, D200, N186, N64, and G63 (Fig. 1B). When binding to FYN, compound **4** was predicted to form 2 total H-bonds with hinge region residues M85 and E83 (Fig. 1C and 1D). Additionally, it was predicted to form hydrophobic contacts between its aminopyrazole core heterocycle and L137, between its cyclopropyl group and residues T82, A37, V67, and A147, between its benzylamine moiety and residues D148, N135, A134, V25, and G18, and between its pyrimidine core moiety and residues L17, G88, N86, and Y84 (Fig. 1D).

Compound **4** was synthesized by applying an easily scalable two-step synthetic procedure (Scheme 1) based on two sequential nucleophilic aromatic substitution (SNAr) reactions on 2,4-dichlorothieno[3,2-*d*]pyrimidine (**1**). Taking advantage of the higher reactivity of 4-heterocycle position, a solvent-free substitution of **1** with 3-cyclopropyl-1*H*-pyrazol-5-amine (**2**), in the presence of triethylamine as base, allowed us to chemoselectively obtain intermediate **3** in very good yields. Remarkably, we employed **2** without performing a preliminary protection of the endocyclic NH of the pyrazole moiety. Intermediate **3** regiochemistry was corroborated through 1D- and 2D-NMR studies (Figs. S1, S2, and S3 of SI), by confirming the different reactivity of the two chlorine atoms at 2 and 4 positions of **1**. Further SNAr of intermediate **3** using an excess of benzylamine in *n*-butanol at 110 °C afforded the target compound **4**.

The inhibitory potency of compound **4** was first evaluated in a human CDK/MAPK/GSK3/CLK (CMGC) Kinase Enzymatic Radiometric Assay and then in HEK293 cells transiently transfected with GSK-3β and FYN NanoLuc Fusion Vector. In the enzymatic assay (performed at Eurofins Cerep, Poitiers, France), **4** showed single-digit nanomolar inhibition vs. both GSK-3β and FYN (IC_{50} = 5 and 3 nM, respectively; Table 1), in excellent agreement with the data reported in the literature [25].

The NanoBRET binding assay (Table 1) was performed at Reaction Biology (PA, USA) to evaluate the apparent binding affinity and permeability of compound **4** by competitive displacement of a NanoBRET tracer reversibly bound to a NanoLuc fusion protein in cells. In this assay, CHIR-99021 and Dasatinib were selected as reference compounds for GSK-3β and FYN, respectively. Remarkably, the compound displayed a kinase-inhibitor-like occupancy in the nanomolar range for both enzymes (IC_{50} = 9.65 nM for GSK-3β and 91.1 nM for FYN; Table 1). In both cases, mainly against FYN, lower binding affinities were observed in comparison with the inhibition potency of the enzymatic assay, suggesting an influence of the cellular environment on the potency profile of the compound.

Crystallographic studies were also performed to confirm the computational poses and identify the essential structural features for binding to GSK-3β and FYN. GSK3β–**4** crystals were diffracted to a resolution of about 2.6 Å (PDB ID: 7OY5, Fig. 2). Molecular

replacement analysis located two protein molecules in the asymmetric unit. Unambiguous positive electron density, corresponding to our compound **4**, was observed in the ATP binding site of GSK-3β (Fig. 2A and B). In the refined structure, **4** displays H-bond interactions with backbone atoms of the hinge region residues of ASP133 and VAL135 (Fig. 2C) in agreement with the initial docking simulations (Fig. 1A and 1B). Moreover, compound **4** occupies the ATP pocket in "DFG-in" conformation making it consistent with type-I inhibition.

Despite several efforts, all attempts to crystallize compound **4** with human FYN-T protein proved unsuccessful due to poor sample homogeneity. Different patterns of phosphorylation of the protein most likely induced sample heterogeneity, thus preventing the formation of good diffracting crystals.

Therefore, we overlapped the available X-ray structure of FYN (PDB ID: 2DQ7) with the in-house generated GSK3β–**4** crystal structure taking advantage of their high homology (Fig. 3). According to the overlapped structure, compound **4** may be lodged in the hinge region of FYN adopting a bound conformation very similar to that observed at the GSK-3β ATP binding pocket (Fig. 3A) and able to establish H-bond interactions with GLU83 and MET85 backbone residues (Fig. 3B). The binding arrangement of **4** inside the FYN ATP binding pocket, deduced from 3D structures superposition, agrees with the structural information obtained from the docking model (FYN-**4**). Like GSK3β, compound **4** is likely to adopt type-I inhibition for FYN too.

In line with the well-balanced and potent dual inhibitory activity against both GSK-3β and FYN, we decided to investigate compound **4**'s ability to reduce tau hyperphosphorylation in a fluorescence bundle formation assay in a human recombinant U2OS cell line, which stably expresses triple mutant (TM) tau 0N4R (Tau0N4R-TM-tGFP line).

The binding of tau protein to MTs and consequent bundle-formation are two processes dependent on the phosphorylation of tau protein. High phosphorylation levels lead to tau dissociation from MTs and their aggregation into tangles of paired helical filaments (PHF). In contrast, tau kinase inhibitors or phosphatase activators promote tau binding to MTs and the formation of MT bundles. In this cell-based assay carried out at Innoprot (Spain), Medium (OptiMem) and Vehicle (DMSO) were used as negative controls, and the well-known GSK-3β inhibitor LiCl was employed as a positive control at 30 mM concentration. The bundle increase was monitored and quantified by fluorescence using automated image analysis (Fig. 4B). As reported in Figure 4A, our compound showed a dose-dependent effect in the range of 0.5–10 μM concentrations, and, at 10 μM concentration, a maximum increase in the bundle formation of almost 11 times was observed (as compared to the negative control). Moreover, at 2.5 μM our compound proved to be 1.4-fold more active than LiCl in reducing tau phosphorylation. At higher concentrations (25–100 μM), cytotoxicity effects started to appear, likely because of an excessive reduction of tau phosphorylation which can lead to cell death for MTs destabilization (Fig. 4A and 4B).

Given these encouraging results and considering the high degree of homology of PKs catalytic sites, we performed a preliminary assessment of compound **4**'s selectivity at 0.1

and 10 μM concentrations *versus* a small panel of 20 different PKs (reported in the kinome tree, see Figure 5), selected according to their phylogenetic similarity to GSK-3β and FYN, and the involvement in tau hyperphosphorylation. In the radiometric kinase activity assay, **4** showed a good selectivity at 0.1 μM as it effectively inhibited GSK-3β and FYN by decreasing 94% and 100% kinase activities, respectively (Table 2), compared to only marginal or weak inhibition against about half of the kinases in the test panel at the same concentration. However, low selectivity was observed relative to some PKs phylogenetically correlated to GSK-3β and FYN, such as GSK-3α and Yes (Table 2).

An unexpected, yet beneficial activity against DYRK1A and CDK5/p25, two additional PKs related to tau hyperphosphorylation, was observed at 10 μM (92% and 97% inhibition, respectively), suggesting a beneficial effect of both PKs inhibition by **4** for purposes of tau hyperphosphorylation decrease and reversal of tauopathies. Based on these outcomes, we aimed to widen the multikinase profile of **4** from a dual GSK-3β/FYN to a triple PK inhibitor. We thus ranked all the PKs from the selectivity panel to find the most suitable one to tackle tauopathyrelated diseases. We assigned a score to each PK between 0 and 1, representing an informed estimation of the strength of association between each target and the disease. We particularly focused on CNS neurodegenerative diseases, brain development, and neuromuscular disorders by using the data reported in Open Targets Platform [27], an open access tool that supports systematic identification and prioritization of potential drug targets.

As depicted in Table 2, DYRK1A and CDK5/p25, belonging to the same CMGC group of Ser/Thr kinases (Figure 5), were identified along with GSK-3β and FYN as the top four most relevant PKs [6, 28].

Cyclin-dependent kinase 5 (CDK5) is a proline-directed Ser/Thr kinase, which belongs to the CDK family. It is predominantly located in postmitotic neurons, where it plays a vital role in brain development, neuronal survival, synaptic plasticity, microtubule regulation, and pain signaling. Under neurotoxic conditions, p25, the *N*-terminal truncated isoform of p35, promotes CDK5 hyperactivation leading to tau hyperphosphorylation and consequent aggregation to form NFTs in AD [30, 31].

Dual-specificity tyrosine phosphorylation-regulated kinase 1A (DYRK1A) is a member of the dual-specificity protein kinase (DYRK kinases) family, characterized by Ser and Thr phosphorylation activity as well as autophosphorylation activity on Tyr residues[32, 33]. The DYRK1A gene is located on chromosome 21 (21q22.2), a region known as the Down-Syndrome Critical Region (DSCR), and its product of expression has been recognized to play a critical role in neural proliferation and neurogenesis of the developing brain. As the CDK5/p25 isoform, abnormal expression of DYRK1A has been found in AD, Down syndrome, Pick disease patients, and related transgenic models [34].

Considering the high values of percentage inhibition at 0.1 μM concentration, we first determined the IC_{50} values of compound **4** for both DYRK1A and CDK5/p25. Then, we performed docking and X-ray studies to identify the structural features of our compound responsible for the reductions in both enzymes' activities. In the enzymatic radiometric

assay, our compound **4** showed 0.9 μM inhibitory potency against DYRK1A and proved to inhibit CDK5/p25 with an IC_{50} value of 40 nM (Table 3). Compound **4** was then docked against flexible receptor models of DYRK1A and CDK5 and binding scores of −26.5 and −21.1 were calculated for DRYK1A and CDK5, respectively. Moreover, crucial contacts between our compound and key residues in the ATP-binding sites of both proteins (Fig. 6) were observed, resembling those typical of type I or II inhibitors [26]. In detail, the aminopyrazole heterocycle in the core region of **4** was predicted to form 3 H-bonds with hinge region residues L241 and E239 when binding to DYRK1A (Fig. 6A) and 3 total H-bonds with hinge region residues C83 and E81 when binding to CDK5 (Fig. 6C). When binding to DYRK1A, compound **4** was predicted to form hydrophobic interactions between its pyrimidine core moiety and residues E291, N244, D247, Y243, and S242, its aminopyrazole heterocycle and residues M240, F239, and A186, its cyclopropyl group and residues F238, V222, and V173, and between its benzylamine moiety and residues V173, G166, F170, and V306 (Fig. 6B). When binding to CDK5, compound **4** was predicted to form hydrophobic contacts between its pyrimidine core moiety and residues I10, Q85, L133, and D84, between its aminopyrzole heterocycle moiety and residues F82 and A31, its cyclopropyl group and residues F80, V64, and K33, and between its benzylamine moiety and residues E12, G13, D144, N131, Q130, and D86 (Fig. 6D).

To corroborate the docking results, we soaked DYRK1A crystals with **4** (Fig. 7, PDB ID: 7OY6). The crystals diffracted at 2.4 Å resolution, and, according to molecular replacement analysis, a single protein molecule was found located in the asymmetric unit. A clear electron density corresponding to compound **4** was observed in the ATP binding pocket (Fig. 7A and 7B), as reported above for GSK-3β. Similar to GSK-3β in complex with our compound, and in good agreement with docking simulations, **4**-DYRK1A complex displayed H-bond interactions with backbone atoms of the hinge region residues GLU239 and LEU241 (Fig. 7C). Like GSK-3β, here also compound **4** demonstrates type-I inhibition in the ATP binding pocket.

As for CDK5/p25, we overlapped the available X-ray structure of CDK5 (PDB ID: 1UNL) with the X-ray structure of GSK-3β in complex with **4** (Fig. 8). According to the structural overlapping, **4** adopted a binding pose like that observed at the ATP GSK-3β binding site (Fig. 8A). Compound **4** is likely to form key H-bond interactions with backbone atoms of CDK5 residues (GLU81 and CYS83, Fig. 8B) as previously observed for the other kinases (Figs. 2, 3, and 7). Here too, the excellent agreement between this structure and that coming from docking simulations testify to the high reliability of the *in silico* studies. Given this, it is highly likely that compound **4** will be a type-I inhibitor also for CDK5/p25 as well.

Despite numerous past efforts to find agents able to modulate aberrant CDK5 activity linked to AD and related tauopathies, several CDK5 inhibitors have not shown selectivity relative to other CDKs involved in the cell cycle and mRNA transcription regulation. Additionally, the development of CDK5 inhibitors as promising CNS drug candidates has been hampered by severe off-target adverse effects [31, 35]. Conversely, DYRK1A is a relatively recent and promising PK to tackle neurodegenerative disorders such as AD (including early-onset AD in Down's syndrome patients) and Parkinson's disease (PD) [36–38]. This enzyme phosphorylates tau at 11 different Ser/Thr sites, including Thr212 as the predominant one

[39]. Phosphorylation at Thr212 promotes further phosphorylation of tau at Ser208 by GSK-3β *in vitro*, suggesting a crucial role for DYRK1A in priming phosphorylation of GSK-3β substrates [40]. Moreover, DYRK1A by phosphorylation of proline-rich domain splicing factor SRp55 (Ser/arginine (Arg)-rich protein 55) and Ser227, Ser234, and Ser238 alternative splicing factor (ASF) is involved in suppression of tau exon 10 inclusion and consequent generation of tau isoforms with three- or four-MT binding repeats, namely 3R-tau and 4R-tau, whose imbalance in adult brains has been associated with tau protein aggregation and NFTs-related degeneration [41, 42].

Based on these considerations, we selected DYRK1A as the third kinase to be inhibited simultaneously with GSK-3β and FYN to tackle aberrant tau hyperphosphorylation. To maintain consistency with FYN and GSK-3β, we employed the NanoBRET assay to confirm the capability of compound **4** to bind to DYRK1A in HEK293 cells. As reported in Table 3, although with less affinity than observed for FYN and GSK-3β, our compound proved to engage DYRK1A with an IC_{50} value in the low micromolar range. Again, the potency was lower than that observed in the enzymatic biochemical assays, possibly due to an effect of the cellular environment on **4**'s apparent binding affinity for the enzyme.

CONCLUSIONS

We report here the synthesis and characterization of **ARN25068 (4)** as a low nanomolar inhibitor of GSK-3β and FYN that displayed an attractive inhibitory potency against DYRK1A in the sub-micromolar range. Computational and X-ray studies allowed us to elucidate the key structural elements for establishing H-bond and hydrophobic interactions with specific residues at the ATP-binding sites of all three PKs. Moreover, in NanoBRET binding assays, the same compound showed permeability in HEK293 cells and binding affinities in the nanomolar range for both GSK3β and FYN and in the single-digit micromolar range for DYRK1A.

Remarkably, at 10 μM, **4** significantly reduced tau hyperphosphorylation and promoted MT bundles formation in a fluorescence assay on the human recombinant U2OS cell line.

Considering these outcomes, compound **4** holds a great potential as multikinase inhibitor with specific beneficial target profile and has been identified as an attractive hit compound for further investigations and SAR explorations. We are currently designing and synthesizing new series of **4** analogs as first-in-class GSK-3β/FYN/DYRK1A triple inhibitors endowed with potent and well-balanced inhibitory activity and improved selectivity, with the ultimate objective of discovering innovative CNS tools for tauopathies and related disorders.

EXPERIMENTAL SECTION

General information.

Solvents and reagents were obtained from commercial suppliers and were used without further purification. Thin-layer chromatography analyses were performed using pre-coated Supelco silica gel on TLC Al foils 0.2 mm and visualized by UV (254 nm). Automated column chromatography purifications were done using a Teledyne ISCO apparatus

(CombiFlash® Rf) with pre-packed silica gel columns of different sizes (from 4 g until 24 g). Mixtures of increasing polarity of CH_2Cl_2 and CH_2Cl_2/MeOH 9:1 were used as eluents.

NMR experiments were run on a Bruker Avance III 400 system (400.13 MHz for ^1H), equipped with a BBI probe and Z-gradients and on a Bruker Avance III 600 MHz spectrometer 100.62 MHz (151 MHz for ^{13}C), equipped with a 5 mm CryoProbeTM QCI 1H/19F– 13C/15N–D quadruple resonance, a shielded z-gradient coil and the automatic sample changer SampleJetTM NMR system. Spectra were acquired at 300 K, using deuterated dimethylsulfoxide (DMSO-d_6) and acetone (Acetone-d_6) as solvents. Chemical shifts for ^1H and ^{13}C spectra were recorded in parts per million using the residual non-deuterated solvent as the internal standard (for DMSO-d_6: 2.50 ppm, ^1H; 39.52 ppm, ^{13}C). Data are reported as follows: chemical shift (ppm), multiplicity (indicated as: br., broad signal; s, singlet; d, doublet; t triplet; dd doublet of doublets, doublet of quartets; m, multiplet and combinations thereof), coupling constants (*J*) in Hertz (Hz) and integrated intensity.

UPLC/MS analyses were run on a Waters ACQUITY UPLC/MS system consisting of a SQD (Single Quadropole Detector) Mass Spectrometer equipped with an Electrospray Ionization interface and a Photodiode Array Detector. The PDA range was 210–400nm. The analyses were performed on an ACQUITY UPLC BEH C_{18} (50×2.1 mmID, particle size 1.7μm) with a VanGuard BEH C_{18} pre-column (5×2.1 mmID, particle size 1.7 μm). The mobile phase was 10 mM NH_4OAc in H_2O at pH 5 adjusted with AcOH (A) and 10 mM NH_4OAc in ACN-H_2O (95:5) at pH 5 (B). Electrospray ionization in positive and negative mode was applied in the mass scan range 100–750 Da. UPLC-MS analyses were performed by applying a generic method where the mobile phase B was increased from 5% to 95% in 2.5 min.

The quality control (QC) analysis of the final compound was performed on a Waters ACQUITY UPLC/MS system consisting of a SQD (single quadrupole detector) mass spectrometer equipped with an electrospray ionization interface and a photodiode array detector. Electrospray ionization in positive and negative mode was applied in the mass scan range 110–750 Da and the PDA range was 210–400 nm. The analysis was run on an ACQUITY UPLC BEH C_{18} (100×2.1 mmID, particle size 1.7μm) with a VanGuard BEH C_{18} pre-column (5×2.1 mm ID, particle size 1.7 μm), using 10 mM NH_4OAc in H_2O at pH 5 adjusted with AcOH (A) and 10 mM NH_4OAc in ACN-H_2O (95:5) at pH 5 (B) as mobile phase. A linear gradient was applied starting from 10% of the mobile phase B, holding for 0.20 min. Then increasing B from 10% to 90% in 6 min 90–100%B in 0.10 min and 100% B hold for 0.70 min with a total run time of 7 min.

Compounds were named using the naming algorithm developed by CambridgeSoft Corporation and used in ChemDraw professional 20.0.

Synthesis of 2-chloro-*N*-(5-cyclopropyl-1*H*-pyrazol-3-yl)thieno[3,2-*d*]pyrimidin-4-amine (3).

Triethylamine (0.748 ml, 5.363 mmol) was added to a mixture of 0.500 g (2.438 mmol) of 2,4-dichlorothieno[3,2-*d*]pyrimidine (**1**) and 0.751 g (6.094 mmol) of 3-cyclopropyl-1*H*-pyrazol-5-amine (**2**). The resultant mix was allowed to react at room temperature for 72

hrs under an inert atmosphere (Ar). After complete conversion of the starting material, the reaction mixture was poured into water (10 ml) and filtrated. A final trituration of the isolated solid by using ACN (7 ml) afforded intermediate **3** as a white powder (556 mg, 78% yield). UPLC-MS: Rt = 1.69 min, MS (ESI) *m/z*: 292.4/294.1 [M+H]$^+$, $C_{12}H_{11}ClN_5S^+$ [M+H]$^+$ calculated: 292.0/294.0.

^{1}H NMR (400 MHz, DMSO-d_6) δ 12.41 (br. s, 1H, H10), 10.46 (br. s, 1H, H12), 8.19 (d, *J* = 5.4 Hz, 1H, H8), 7.34 (d, *J* = 5.4 Hz, 1H, H7), 6.24 (br. s, 1H, H15), 1.93 (dq, *J* = 5.1, 1.5 Hz, 1H, H16), 0.95 (dd, *J* = 4.1, 1.8, 2H, H17 or H18) 0.72 (dd, *J* = 4.1, 1.8 Hz, 2H, H17 or H18). (Figs. S1 and S3 of SI).

^{13}C NMR (151 MHz, DMSO-d_6) δ 161.81 (C6), 155.94 (C2, C4), 146.12 (C11), 145.81 (C14), 136.63 (C7), 123.04 (C8), 113.38 (C5), 96.51 (C15), 7.81 (C17, C18), 6.83 (C16). (Figs. S2 and S3 of SI).

Synthesis of *N*2-benzyl-*N*4-(5-cyclopropyl-1*H*-pyrazol-3-yl)thieno[3,2-*d*]pyrimidine-2,4-diamine (ARN25068, 4).

0.556 g (1.905 mmol) of **3** and 1.042 ml of benzylamine (9.527 mmol) were dissolved in 6.35 ml of *n*-butanol. The reaction mixture was heated up to 110 °C and was stirred at the same temperature for days an under inert atmosphere (Ar). After observing starting material complete conversion, the reaction mixture was cooled down to room temperature and was concentrated to dryness. The resulting crude was purified by normal phase flash chromatography by employing a 12 g gold silica cartridge (Solvent A: CH_2Cl_2 -Solvent B: CH_2Cl_2/EtOH 9:1 -Detection: 240/260 nm - Gradient: 10–40% solvent B). A final trituration by using CH_2Cl_2 (7 ml) yielded the desired product as a white powder (466 mg, 68% yield). UPLC-MS: Rt = 1.89 min, MS (ESI) *m/z*: 363.1 [M+H]$^+$, $C_{19}H_{19}N_6S^+$ [M+H]$^+$ calculated: 363.1. QC analysis: Rt = 3.74 min, UPLC-MS purity (UV at 215 nm): 99 %. (Fig. S8 and S9 of SI)

Both ^{1}H- and ^{13}C-NMR spectra in DMSO-d_6 were consistent with the isolation of two different tautomeric forms **a** and **b** in a dynamic equilibrium as described below (Figs. S5 and S7 of SI); however, in acetone-d_6 the presence of only one tautomeric form consistent with **a** was observed (Fig. S5 of SI).

^{1}H NMR (400 MHz, DMSO-d_6) δ 12.57 (br. s, 1Hb), 12.07 (br. s, 1Ha), 10.26 (br.s, 1Hb), 9.60 (br.s, 1Ha), 7.90 (br. s, 1Ha), 7.68 (br. s, 1Hb), 7.46 – 6.90 (m, 7Ha, 7Hb), 6.34 (s, 1Ha), 5.66 (s, 1Hb), 4.55 (d, *J* = 6.2 Hz, 2Ha, 2Hb), 1.83 (dq, *J* = 1.2, 4.9 Hz, 1Ha, 1Hb), 0.87 (br. s, 2Ha, 2Hb), 0.63 (br. s, 2Ha, 2Hb). (Fig. S5 of SI).

^{1}H NMR (400 MHz, acetone-d_6) δ 11.73 (br. s 1H), δ 8.92 (br. s 1H), 7.84 (d, *J* = 5.4 Hz, 1H), 7.43 7. (d, *J* = 7.29, 1H), 7.30 (t, *J* = 7.5 Hz, 2H), 7.22 (t, *J* = 7.3 Hz, 1H), 7.08 (d, *J* = 5.4 Hz, 1H), 6.72 (s, 1H), 6.72 (br. s, 1H), 6.12 (br. s, 1H) 4.71 (d, *J* = 6.0 Hz, 2H), 1.87 (tq, *J* = 5.1, 1.65 Hz, 1H), 0.86 (dd, *J* = 4.21, 2.0 Hz, 2H), 0.66 (dd, *J* = 4.15, 2.2 Hz, 2H). (Fig. S6 of SI).

^{13}C NMR (151 MHz, DMSO-d_6) δ 162.30, 160.60, 154.72, 153.05, 152.28, 147.43, 145.12, 141.08, 140.18, 133.14, 128.04, 126.80, 126.23, 123.34, 122.83, 105.36, 94.90, 88.41, 44.13, 9.22, 7.61, 6.75. (Fig. S7 of SI).

Human CMGC Kinase Enzymatic Radiometric Assay [Km ATP], KinaseProfiler.

h-Fyn is incubated with 50 mM Tris pH 7.5, 0.1 mM EGTA, 0.1 mM Na$_3$VO$_4$, 250 μM KVEKIGEGTYGVVYK (Cdc2 peptide), 10 mM Magnesium Acetate and [gamma-33P]-ATP (specific activity and concentration as required). The reaction is initiated by the addition of the Mg/ATP mix. After incubation for 40 minutes at room temperature, the reaction is stopped by the addition of phosphoric acid to a concentration of 0.5%. An aliquot of the reaction is then spotted onto a filter and washed four times for 4 minutes in 0.425% phosphoric acid and once in methanol prior to drying and scintillation counting.

h-GSK-3β is incubated with 8 mM MOPS pH 7.0, 0.2 mM EDTA, 20 μM YRRAAVPPSPSLSRHSSPHQS(p) EDEEE (phospho GS2 peptide), 10 mM Magnesium Acetate and [gamma-33P]-ATP (specific activity and concentration as required). The reaction is initiated by the addition of the Mg/ATP mix. After incubation for 40 minutes at room temperature, the reaction is stopped by the addition of phosphoric acid to a concentration of 0.5%. An aliquot of the reaction is then spotted onto a filter and washed four times for 4 minutes in 0.425% phosphoric acid and once in methanol prior to drying and scintillation counting.

h-DYRK1A is incubated with 8 mM MOPS pH 7.0, 0.2 mM EDTA, 50 μM RRRFRPASPLRGPPK, 10 mM Magnesium Acetate and [gamma-33P]-ATP (specific activity and concentration as required). The reaction is initiated by the addition of the Mg/ATP mix. After incubation for 40 minutes at room temperature, the reaction is stopped by the addition of phosphoric acid to 21 a concentration of 0.5%. An aliquot of the reaction is then spotted onto a filter and washed four times for 4 minutes in 0.425% phosphoric acid and once in methanol prior to drying and scintillation counting.

h-CDK5/p25 is incubated with 8 mM MOPS pH 7.0, 0.2 mM EDTA, 0.1 mg/mL histone H1, 10 mM Magnesium Acetate and [g- 33P]-ATP (specific activity and concentration as required). The reaction is initiated by the addition of the Mg/ATP mix. After incubation for 40 minutes at room temperature, the reaction is stopped by the addition of phosphoric acid to a concentration of 0.5%. An aliquot of the reaction is then spotted onto a filter and washed four times for 4 minutes in 0.425% phosphoric acid and once in methanol prior to drying and scintillation counting.

For all tested PKs the Pan-kinase inhibitor Staurosporine was used as a reference compound.

Cellular kinase NanoBRET™ Assay.

HEK293 cells were purchased from ATCC. FuGENEHD Transfection Reagent, Kinase-NanoLucfusion plasmids, Transfection Carrier DNA, NanoBRETTracers and dilution buffer, NanoBRETNano-Glo Substrate, Extracellular NanoLucInhibitor were obtained from Promega. All compounds were purchased from Selleckchem.

Assays were conducted following Promega assay protocol with some modifications. HEK293 Cells were transiently transfected with Kinase-NanoLucFusion Vector DNA by FuGENEHD Transfection Reagent. Testing compounds were delivered into 384 well assay plate by Echo 550 (LabcyteInc, Sunnyvale, CA). Transfected cells were harvested and mixed with NanoBRETTracer Reagent and dispensed into 384 well plates and incubated the plates at 37 °C in 5% CO_2 cell culture incubator for 1 hour. The NanoBRETNano-Glo Substrate plus Extracellular NanoLucInhibitor Solution were added into the wells of the assay plate and incubated for 2–3 minutes at room temperature. The donor emission wavelength (460 nm) and acceptor emission wavelength (600 nm) were measured in the EnVisionplate reader. The BRET Ratio were calculated. BRET Ratio = [(Acceptor sample÷Donor sample)–(Acceptor no-tracer control÷Donor no-tracer control)]. The IC_{50} values of compounds were calculated with Prism GraphPad program.

Tau Phosphorylation Assay in human recombinant Tau0N4R-TM-tGFP U2OS cells.

Dose-response for test compound was performed using a cellular fluorescence bundle formation assay after compound addition in human recombinant Tau0N4R-TM-tGFP U2OS stable cell line. The formation of tau and microtubule bundles after treatment was measured in triplicate. Medium (OptiMem) and Vehicle (DMSO) were used as negative controls and LiCl 30 mM as positive control. Bundles were quantified using the Cell Insight CX7 from Thermofisher. The error bars represent the standard deviation among the 3 replicate wells.

GSK-3β and DYRK1A expression and purification.

Human full-length GSK-3β sequence (1–400) was overexpressed in high 5 insect cells as previously described.[43] For purification a cell pellet of 900×10^6 cells was thawed and resuspended in lysis buffer (20 mM TRIS pH 8.0, 0.5 M NaCl, 10 mM imidazole, 1 mM DTT, 5 mM $MgCl_2$, 0.5x protease inhibitor EDTA free *(Roche),* 5% glycerol, 0.01% Tween20) and lysed by sonication (12' pulse at 60–70% intensity). After sonication, lysate solution was incubated for 20 minutes at 4 °C with DNAseI (5 μg/mL final working concentration), and centrifuged for 1 hr at 30000 g in 4 °C. The supernatant solution, containing the protein of interest, was used for further purification. First, the clarified supernatant was incubated for 2 hrs with Ni-NTA agarose resin (Qiagen). The protein bound resin was washed with binding buffer (20 mM TRIS pH 8.0, 0.5 M NaCl, 10 mM Imidazole, 5% glycerol, 1 mM DTT). Protein elution was obtained by addition of 300 mM Imidazole to the binding buffer. Eluted protein solution was further purified using a cationic exchange column *HiTrap HP SP,* equilibrated with buffer A (20 mM Hepes pH 7.5, 40 mM NaCl, 5% glycerol, 1 mM DTT). Different isoforms, corresponding to different GSK3β phosphorylation states, were separated by applying a linear gradient to Buffer B (20 mM Hepes pH 7.5, 1 M NaCl, 5% glycerol, 1 mM DTT). The GSK-3β isoforms were separately collected and stored at −80 °C.

For DYRK1A, a pET28a vector, inserted with codon optimized C-DNA sequence (coding for DYRK1A kinase domain residue 127–485) between NcoI/XhoI site was used. The expressed DYRK1A Kinase domain, contained a *N*-terminal Hexa-His tag separated from the protein by a 3C protease cleavage tag. *E.coli* cells (BL21DE3) transfected with this vector, were used to overexpress the protein. Briefly, an overnight culture was used to

inoculate 1 L Luria-Bertani (LB) medium supplemented with 50 μM kanamycin. Protein overexpression was induced by addition of 0.5 mM IPTG when OD_{600} reached 0.6. After overnight bacteria growth at 25 °C, cells were pelleted, and lysis was performed in 50 mM potassium phosphate pH 7.4, 500 mM NaCl, 1 mM DTT, 5% glycerol, 0.5x protease inhibitor (EDTA free) using sonication. The first purification step was a His-trap affinity chromatography using the equilibration buffer: 50 mM potassium phosphate pH 7.4, 500 mM NaCl, 1 mM DTT, 5% glycerol and 5 mM imidazole. After an initial wash with the 25 mM imidazole buffer, the elution was performed using 200 mM imidazole. Histag was removed by overnight incubation of the purified protein with 3C protease at 4 °C. His-trap affinity chromatography was then run, to remove the un-cleaved protein and the His-Tag. The final purification step was performed with a Superdex 200 increase (GE Healthcare) column with the following running buffer: 50 mM Mes 6.5, 100 mM KCl, 1 mM DTT and 5% glycerol. The purified protein was finally stored at −80 °C.

Computational modeling and chemical docking.

Multiple relevant published structures of each of the human proteins GSK-3β, CDK5, DYR1A, and FYN were obtained from PDB and combined into conformational stacks using ICM pro software, version 3.9–2b. From these stacks, flexible receptor 4D grids were generated, and compound **4** was docked *in silico*. Binding scores representing Gibbs free energy were calculated, also using ICM pro [44].

GSK-3β and DYRK1A crystallization, data collection and processing.

GSK-3β protein was mixed with compound **4** (1–2 mM final concentration), and later concentrated to a 2–3 mg/ml final protein concentration in 20 mM hepes 7.5, 200 mM NaCl, 5% glycerol, 1 mM DTT buffer. Complex crystallization was performed using hanging drop vapor diffusion method. Drops were prepared by mixing 1μl of protein solution with 1 μl of reservoir solution (20 mM hepes 7.5, 15–20% polyethylene glycol 3350, 50 mM $MgCl_2$). Crystals appeared in one day and grew in size for one week. Crystals were soaked in the reservoir buffer supplemented with 20% glycerol before freezing in liquid nitrogen.

DYRK1A crystallization was also performed with the hanging drop method. Final protein concentration was 4–5 mg/ml in 50 mM Mes 6.5, 100 mM KCl, 1 mM DTT, 5% glycerol, while reservoir buffer was 50 mM Mes 6.5, 150 mM KCl, 15–20% polyethylene glycol 1000. Protein solution was mixed with the reservoir buffer in a 1:1 ratio, and equilibrated against the reservoir buffer. Crystals appeared in one day and grew for a weak. Crystals were soaked for 5–6 hrs in 50 mM Mes 6.5, 150 mM KCl, 20% PEG 1000 buffer and 1–2 mM of **4**. Crystals were later frozen in liquid nitrogen.

X-ray diffraction data were collected at the XRD2 beamline in Elettra Synchrotron, Trieste, Italy. Data integration was performed using iMOSFLM in CCP4 [45]. Scaling is performed using AIMLESS [46]. Structures were solved by molecular replacement PHASER in CCP4 [47]. For molecular replacement the following available structures were used: PDB ID 6H0U (GSK3β) and 3ANQ (DYRK1A). Structures were refined using REFMAC [48]. Model modification, visualization and evaluation were performed using Coot [49]. Images were prepared using Pymol [50]. Data processing statistics are compiled in Table S1 of

SI. PDB IDs of submitted GSK-3β and DYRK1A are: 7OY5 for GSK-3β and 7OY6 for DYRK1A.

Supplementary Material

Refer to Web version on PubMed Central for supplementary material.

ACKNOWLEDGMENT

Funding

ABBREVIATIONS

ACN	acetonitrile
AD	Alzheimer Disease
ASF	alternative splicing factor
***n*-BuOH**	*n*-butanol
CDK5	Cyclin-dependent kinase 5
CLK	CDK-like kinases
CMGC	CDK/MAPK/GSK3/CLK
CNS	central nervous system
DYRK1A	dual-specificity tyrosine phosphorylation-regulated kinase 1A
DMSO	dimethyl sulfoxide
EtOH	ethanol
Et₃N	triethylamine
FTLD	frontal temporal lobar degeneration
GSK-3β	glycogen synthase kinase-3β
HMBC	heteronuclear multiple bond correlation
MAPK	mitogen-activated protein kinase
MT	microtubule
NFTs	neurofibrillary tangles
PHF	paired helical filaments

PKs	protein kinases
SAR	structure–activity relationship
SFKs	Src family kinases
SQD	single quadropole detector
SRp55	Ser/arginine (Arg)-rich protein 55
TK	tyrosine kinase
TLC	thin layer chromatography
TM	triple mutant

REFERENCES

[1]. Manning G, Whyte DB, Martinez R, Hunter T, Sudarsanam S, The Protein Kinase Complement of the Human Genome, Science, 298 (2002) 1912–1934. [PubMed: 12471243]

[2]. Gunosewoyo H, Yu L, Munoz L, Kassiou M, Kinase targets in CNS drug discovery, Future Med Chem, 9 (2017) 303–314. [PubMed: 28176536]

[3]. Wilson LJ, Linley A, Hammond DE, Hood FE, Coulson JM, MacEwan DJ, Ross SJ, Slupsky JR, Smith PD, Eyers PA, Prior IA, New Perspectives, Opportunities, and Challenges in Exploring the Human Protein Kinome, Cancer Res, 78 (2018) 15–29. [PubMed: 29254998]

[4]. Hill E, Wall MJ, Moffat KG, Karikari TK, Understanding the Pathophysiological Actions of Tau Oligomers: A Critical Review of Current Electrophysiological Approaches, Front Mol Neurosci, 13 (2020) 155. [PubMed: 32973448]

[5]. Oukoloff K, Nzou G, Varricchio C, Lucero B, Alle T, Kovalevich J, Monti L, Cornec AS, Yao Y, James MJ, Trojanowski JQ, Lee VM, Smith AB 3rd, Brancale A, Brunden KR, Ballatore C, Evaluation of the Structure-Activity Relationship of Microtubule-Targeting 1,2,4-Triazolo[1,5-a]pyrimidines Identifies New Candidates for Neurodegenerative Tauopathies, J Med Chem, 64 (2021) 1073–1102. [PubMed: 33411523]

[6]. Yadikar H, Torres I, Aiello G, Kurup M, Yang Z, Lin F, Kobeissy F, Yost R, Wang KK, Screening of tau protein kinase inhibitors in a tauopathy-relevant cell-based model of tau hyperphosphorylation and oligomerization, PLoS One, 15 (2020) e0224952.

[7]. Demuro S, Di Martino RMC, Ortega JA, Cavalli A, GSK-3beta, FYN, and DYRK1A: Master Regulators in Neurodegenerative Pathways, Int J Mol Sci, 22 (2021) 9098. [PubMed: 34445804]

[8]. Wagner U, Utton M, Gallo JM, Miller CC, Cellular phosphorylation of tau by GSK-3 beta influences tau binding to microtubules and microtubule organisation, J Cell Sci, 109 (Pt 6) (1996) 1537–1543. [PubMed: 8799840]

[9]. Billingsley ML, Kincaid RL, Regulated phosphorylation and dephosphorylation of tau protein: effects on microtubule interaction, intracellular trafficking and neurodegeneration, Biochem J, 323 (1997) 577–591. [PubMed: 9169588]

[10]. Eldar-Finkelman H, Martinez A, GSK-3 Inhibitors: Preclinical and Clinical Focus on CNS, Front Mol Neurosci, 4 (2011) 32. [PubMed: 22065134]

[11]. Rippin I, Eldar-Finkelman H, Mechanisms and Therapeutic Implications of GSK-3 in Treating Neurodegeneration, Cells, 10 (2021) 262. [PubMed: 33572709]

[12]. Choi HJ, Cha SJ, Lee JW, Kim HJ, Kim K, Recent Advances on the Role of GSK3β in the Pathogenesis of Amyotrophic Lateral Sclerosis, Brain Sci, 10 (2020) 675. [PubMed: 32993098]

[13]. Di Martino RMC, Pruccoli L, Bisi A, Gobbi S, Rampa A, Martinez A, Pérez C, Martinez-Gonzalez L, Paglione M, Di Schiavi E, Seghetti F, Tarozzi A, Belluti F, Novel Curcumin-Diethyl Fumarate Hybrid as a Dualistic GSK-3β Inhibitor/Nrf2 Inducer for the Treatment of Parkinson's Disease, ACS Chem Neurosci, 11 (2020) 2728–2740. [PubMed: 32663009]

[14]. Guzman-Martinez L, Maccioni RB, Andrade V, Navarrete LP, Pastor MG, Ramos-Escobar N, Neuroinflammation as a Common Feature of Neurodegenerative Disorders, Front Pharmacol, 10 (2019) 1008. [PubMed: 31572186]

[15]. Kypta RM, Hemming A, Courtneidge SA, Identification and characterization of p59fyn (a src-like protein tyrosine kinase) in normal and polyoma virus transformed cells, EMBO J, 7 (1988) 3837–3844. [PubMed: 3061807]

[16]. Tang SJ, Fesharaki-Zadeh A, Takahashi H, Nies SH, Smith LM, Luo A, Chyung A, Chiasseu M, Strittmatter SM, Fyn kinase inhibition reduces protein aggregation, increases synapse density and improves memory in transgenic and traumatic Tauopathy, Acta Neuropathol Commun, 8 (2020) 96. [PubMed: 32611392]

[17]. Schenone S, Brullo C, Musumeci F, Biava M, Falchi F, Botta M, Fyn kinase in brain diseases and cancer: the search for inhibitors, Curr Med Chem, 18 (2011) 2921–2942. [PubMed: 21651487]

[18]. Poli G, Lapillo M, Granchi C, Caciolla J, Mouawad N, Caligiuri I, Rizzolio F, Langer T, Minutolo F, Tuccinardi T, Binding investigation and preliminary optimisation of the 3-amino-1,2,4-triazin-5(2H)-one core for the development of new Fyn inhibitors, J Enzyme Inhib Med Chem, 33 (2018) 956–961. [PubMed: 29747534]

[19]. Ittner LM, Ke YD, Delerue F, Bi M, Gladbach A, van Eersel J, Wölfing H, Chieng BC, Christie MJ, Napier IA, Eckert A, Staufenbiel M, Hardeman E, Götz J, Dendritic function of tau mediates amyloid-beta toxicity in Alzheimer's disease mouse models, Cell, 142 (2010) 387–397. [PubMed: 20655099]

[20]. Tang X, Feng Y, Ye K, Src-family tyrosine kinase fyn phosphorylates phosphatidylinositol 3-kinase enhancer-activating Akt, preventing its apoptotic cleavage and promoting cell survival, Cell Death Differ, 14 (2007) 368–377. [PubMed: 16841086]

[21]. VandeVrede L, Boxer AL, Polydoro M, Targeting tau: Clinical trials and novel therapeutic approaches, Neurosci Lett, 731 (2020) 134919.

[22]. Holzer M, Schade N, Opitz A, Hilbrich I, Stieler J, Vogel T, Neukel V, Oberstadt M, Totzke F, Schächtele C, Sippl W, Hilgeroth A, Novel Protein Kinase Inhibitors Related to Tau Pathology Modulate Tau Protein-Self Interaction Using a Luciferase Complementation Assay, Molecules, 23 (2018) 2335. [PubMed: 30213139]

[23]. Garuti L, Roberti M, Bottegoni G, Multi-Kinase Inhibitors, Curr Med Chem, 22 (2015) 695712.

[24]. Ramsay RR, Popovic-Nikolic MR, Nikolic K, Uliassi E, Bolognesi ML, A perspective on multitarget drug discovery and design for complex diseases, Clin Transl Med, 7 (2018) 3. [PubMed: 29340951]

[25]. Metz JT, Johnson EF, Soni NB, Merta PJ, Kifle L, Hajduk PJ, Navigating the kinome, Nat Chem Biol, 7 (2011) 200–202. [PubMed: 21336281]

[26]. Zhao Z, Bourne PE, Overview of Current Type I/II Kinase Inhibitors, in: Shapiro P. (eds) Next generation kinase inhibitors, 2018, 1–26.

[27]. Ochoa D, Hercules A, Carmona M, Suveges D, Gonzalez-Uriarte A, Malangone C, Miranda A, Fumis L, Carvalho-Silva D, Spitzer M, Baker J, Ferrer J, Raies A, Razuvayevskaya O, Faulconbridge A, Petsalaki E, Mutowo P, Machlitt-Northen S, Peat G, McAuley E, Ong CK, Mountjoy E, Ghoussaini M, Pierleoni A, Papa E, Pignatelli M, Koscielny G, Karim M, Schwartzentruber J, Hulcoop DG, Dunham I, McDonagh EM, Open Targets Platform: supporting systematic drug-target identification and prioritisation, Nucleic Acids Res, 49 (2021) D1302-D1310.

[28]. Martin L, Latypova X, Wilson CM, Magnaudeix A, Perrin ML, Yardin C, Terro F, Tau protein kinases: involvement in Alzheimer's disease, Ageing Res Rev, 12 (2013) 289–309. [PubMed: 22742992]

[29]. Eid S, Turk S, Volkamer A, Rippmann F, Fulle S, KinMap: a web-based tool for interactive navigation through human kinome data, BMC Bioinform, 18 (2017) 16.

[30]. Shah K, Lahiri DK, Cdk5 activity in the brain - multiple paths of regulation, J Cell Sci, 127 (2014) 2391–2400. [PubMed: 24879856]

[31]. Allnutt AB, Waters AK, Kesari S, Yenugonda VM, Physiological and Pathological Roles of Cdk5: Potential Directions for Therapeutic Targeting in Neurodegenerative Disease, ACS Chem Neurosci, 11 (2020) 1218–1230. [PubMed: 32286796]

[32]. Himpel S, Panzer P, Eirmbter K, Czajkowska H, Sayed M, Packman LC, Blundell T, Kentrup H, Grötzinger J, Joost HG, Becker W, Identification of the autophosphorylation sites and characterization of their effects in the protein kinase DYRK1A, Biochem J, 359 (2001) 497–505. [PubMed: 11672423]

[33]. Arbones ML, Thomazeau A, Nakano-Kobayashi A, Hagiwara M, Delabar JM, DYRK1A and cognition: A lifelong relationship, Pharmacol Ther, 194 (2019) 199–221. [PubMed: 30268771]

[34]. Ferrer I, Barrachina M, Puig B, Martinez de Lagran M, Marti E, Avila J, Dierssen M, Constitutive Dyrk1A is abnormally expressed in Alzheimer disease, Down syndrome, Pick disease, and related transgenic models, Neurobiol Dis, 20 (2005) 392–400. [PubMed: 16242644]

[35]. Koyama T, Yamaotsu N, Nakagome I, Ozawa SI, Yoshida T, Hayakawa D, Hirono S, Multi-step virtual screening to develop selective DYRK1A inhibitors, J Mol Graph Model, 72 (2017) 229–239. [PubMed: 28129593]

[36]. Guedj F, Pereira PL, Najas S, Barallobre MJ, Chabert C, Souchet B, Sebrie C, Verney C, Herault Y, Arbones M, Delabar JM, DYRK1A: a master regulatory protein controlling brain growth, Neurobiol Dis, 46 (2012) 190–203. [PubMed: 22293606]

[37]. Soundararajan M, Roos AK, Savitsky P, Filippakopoulos P, Kettenbach AN, Olsen JV, Gerber SA, Eswaran J, Knapp S, Elkins JM, Structures of Down syndrome kinases, DYRKs, reveal mechanisms of kinase activation and substrate recognition, Structure, 21 (2013) 986–996. [PubMed: 23665168]

[38]. Lee Walmsley D, Murray JB, Dokurno P, Massey AJ, Benwell K, Fiumana A, Foloppe N, Ray S, Smith J, Surgenor AE, Edmonds T, Demarles D, Burbridge M, Cruzalegui F, Kotschy A, Hubbard RE, Fragment-Derived Selective Inhibitors of Dual-Specificity Kinases DYRK1A and DYRK1B, J Med Chem, (2021).

[39]. Liu F, Liang Z, Wegiel J, Hwang YW, Iqbal K, Grundke-Iqbal I, Ramakrishna N, Gong CX, Overexpression of Dyrk1A contributes to neurofibrillary degeneration in Down syndrome, FASEB J, 22 (2008) 3224–3233. [PubMed: 18509201]

[40]. Woods YL, Cohen P, Becker W, Jakes R, Goedert M, Wang X, Proud CG, The kinase DYRK phosphorylates protein-synthesis initiation factor eIF2Bε at Ser539 and the microtubule-associated protein tau at Thr212 for DYRK as a glycogen synthase kinase 3-priming kinase, Biochem J, 355 (2001) 609–615. [PubMed: 11311121]

[41]. Yin X, Jin N, Gu J, Shi J, Zhou J, Gong CX, Iqbal K, Grundke-Iqbal I, Liu F, Dualspecificity tyrosine phosphorylation-regulated kinase 1A (Dyrk1A) modulates serine/arginine-rich protein 55 (SRp55)-promoted Tau exon 10 inclusion, J Biol Chem, 287 (2012) 30497–30506.

[42]. Shi J, Zhang T, Zhou C, Chohan MO, Gu X, Wegiel J, Zhou J, Hwang YW, Iqbal K, Grundke-Iqbal I, Gong CX, Liu F, Increased Dosage of Dyrk1A Alters Alternative Splicing Factor (ASF)-regulated Alternative Splicing of Tau in Down Syndrome, J Biol Chem, 283 (2008) 28660–28669.

[43]. Redenti S, Marcovich I, De Vita T, Perez C, De Zorzi R, Demitri N, Perez DI, Bottegoni G, Bisignano P, Bissaro M, Moro S, Martinez A, Storici P, Spalluto G, Cavalli A, Federico S, A Triazolotriazine-Based Dual GSK-3beta/CK-1delta Ligand as a Potential Neuroprotective Agent Presenting Two Different Mechanisms of Enzymatic Inhibition, ChemMedChem, 14 (2019) 310–314. [PubMed: 30548443]

[44]. Neves MAC, Totrov M, Abagyan R, Docking and scoring with ICM: the benchmarking results and strategies for improvement, J Comput-Aided Mol Des, 26 (2012) 675–686. [PubMed: 22569591]

[45]. Battye TG, Kontogiannis L, Johnson O, Powell HR, Leslie AG, iMOSFLM: a new graphical interface for diffraction-image processing with MOSFLM, Acta Crystallogr D Biol Crystallogr, 67 (2011) 271–281. [PubMed: 21460445]

[46]. Evans PR, Murshudov GN, How good are my data and what is the resolution?, Acta Crystallogr D Biol Crystallogr, 69 (2013) 1204–1214. [PubMed: 23793146]

[47]. McCoy AJ, Grosse-Kunstleve RW, Adams PD, Winn MD, Storoni LC, Read RJ, Phaser crystallographic software, J Appl Crystallogr, 40 (2007) 658–674. [PubMed: 19461840]

[48]. Murshudov GN, Vagin AA, Dodson EJ, Refinement of Macromolecular Structures by the Maximum-Likelihood Method, Acta Crystallogr D Biol Crystallogr, 53 (1997) 240–255. [PubMed: 15299926]

[49]. Emsley P, Lohkamp B, Scott WG, Cowtan K, Features and development of Coot, Acta Crystallogr D Biol Crystallogr, 66 (2010) 486–501. [PubMed: 20383002]

[50]. DeLano WL, The PyMOL Molecular Graphics System, Delano Scientific, San Carlos CA 700, (2002).
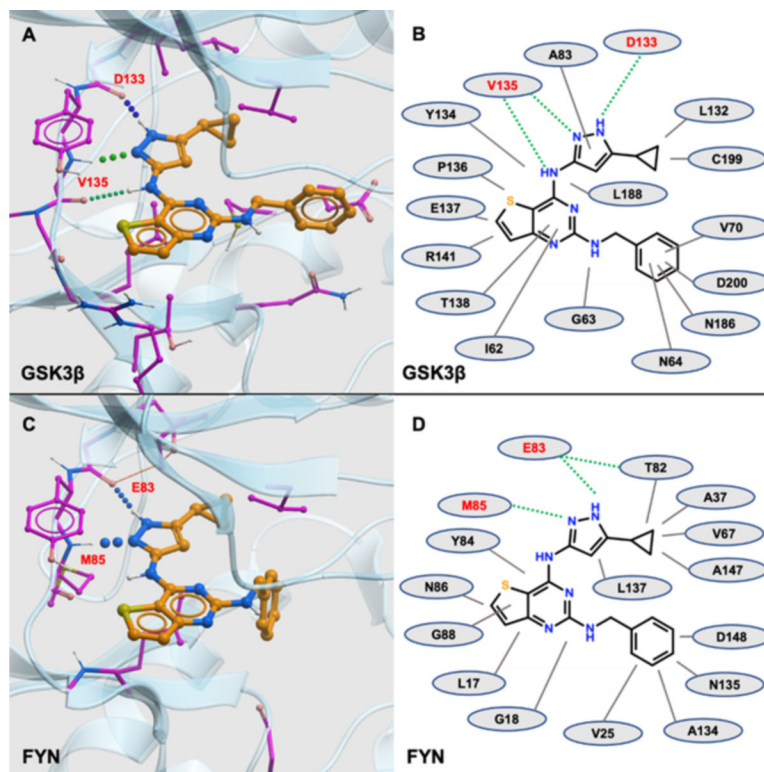
Figure 1.
Graphical representations of the binding mode of **4** to GSK-3β and FYN. (**A, C**) Structural models of the binding sites of GSK-3β (**A**) and FYN (**C**), respectively, showing the binding poses resulting from *in silico* docking simulations. Flexible receptor model for GSK-3β constructed from the following PDB entries: 4IQ6, 4DIT, 4J1R, 4J71, 2OW3, 3GB2, 4PTC, 3M1S, 4PTE, 4PTG, 3SAY, 3SD0, 3I4B, 1PYX, 3DU8, 1Q3D, 1Q3W, 1Q41, 1Q4L, 1Q5K, 2JLD, 1R0E, 3F7Z, 3F88, 1J1B, 1J1C, 2O5K, 3PUP, 5F94, 5F95, 3Q3B, 4ACH, 4ACG, 4ACD, 4ACC, 3L1S. Receptor model for FYN constructed from PDB entry 2DQ7. (**B, D**) Schematics showing the binding pocket interactions predicted between **4** and GSK-3β (**B**) and FYN (**D**), respectively. Hydrophobic interactions are depicted by dark grey lines, and green dotted lines represent hydrogen bonds.
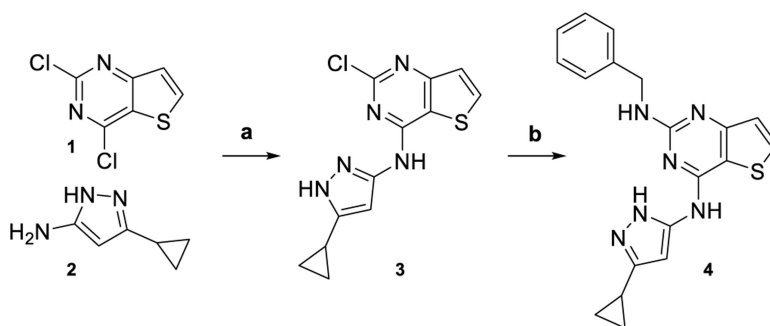
Scheme 1. Synthesis of compound 4.

Reagents and conditions: a) Et₃N (2.2 equiv.), rt, 16 hrs, yield 78%; b) benzylamine (5 equiv.), *n*-BuOH, 110 °C, 72 hrs, yield 68%.
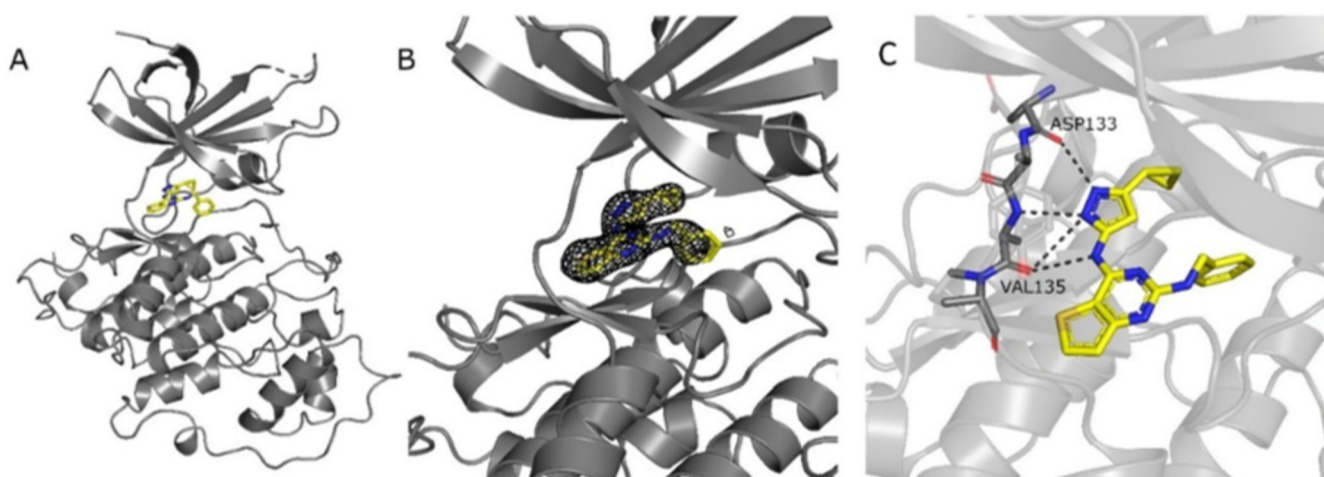
Figure 2.
Crystal structure of GSK-3β with compound **4**. **A.** Compound **4** (yellow) in the ATP binding pocket of GSK-3β (grey). **B.** Electron density map (2F$_O$ - F$_C$) corresponding to **4** is contoured at 1.2σ level (black mesh). **C.** Compound **4** (yellow) displays hydrogen bonding interactions (black dashes) with the hinge region backbone atoms of residues ASP133 and VAL135 of GSK-3β (grey).
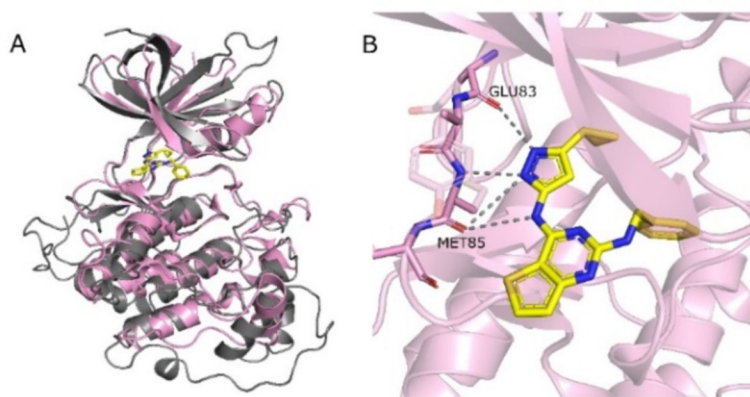
Figure 3.
Overlapping of GSK3β–**4** complex with FYN structure. **A.** Overlapping of FYN (pink) structure (PDB ID: 2DQ7) with the structure of GSK-3β (grey) in complex with **4** (RMSD 2.717). Compound **4** at the ATP binding pocket of FYN. **B.** Potential H-bond interactions (grey dashes) between **4** and FYN backbone atoms (GLU83 and MET85), based on the structures overlapping.
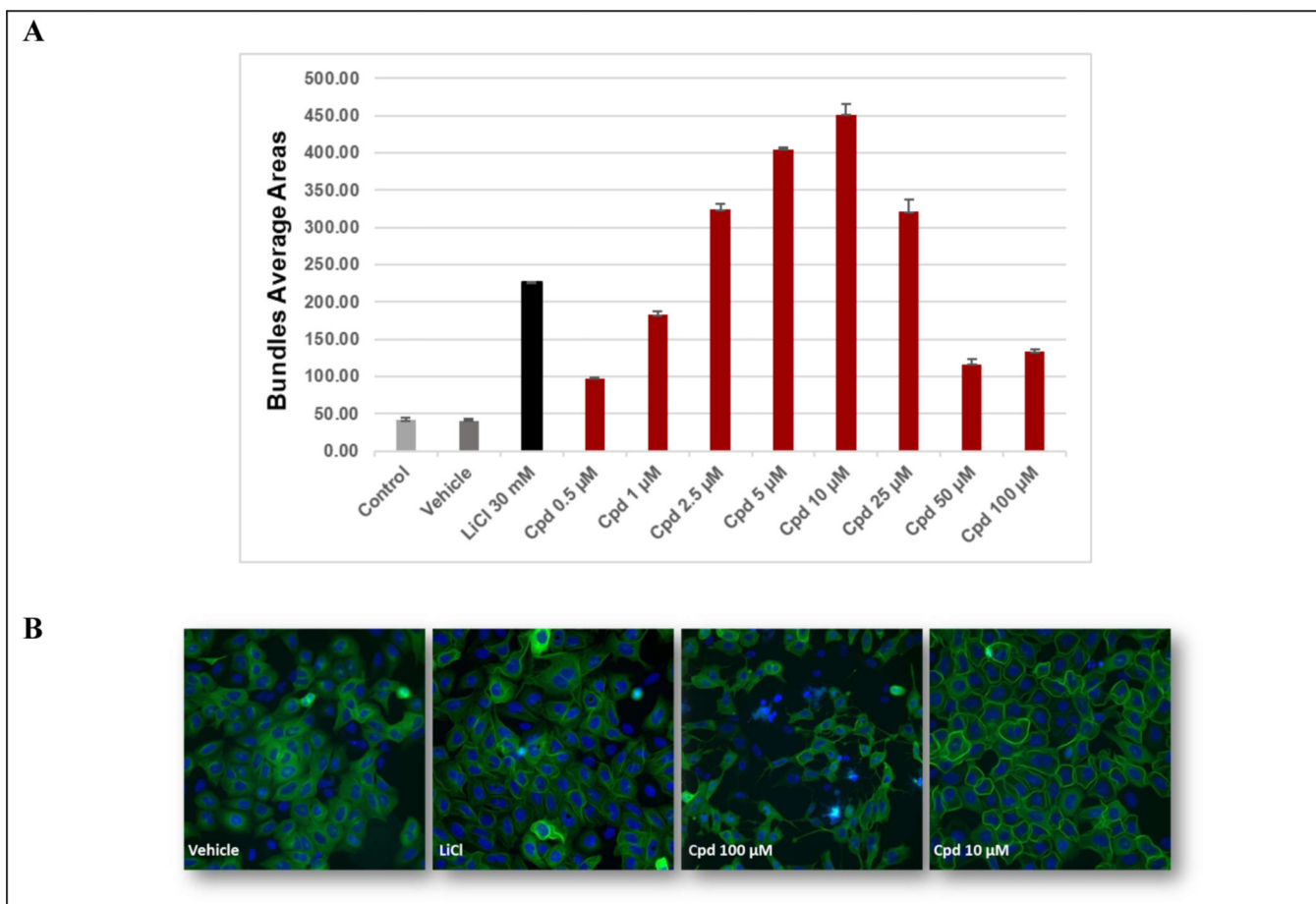
Figure 4:

A. Dose-response relationship for compound **4** (0.5–100 μM), medium (control), vehicle and LiCl (30 mM). Cells were treated with the indicated concentrations for 6 hrs. Data points represent the mean ± SD for each condition for a single experiment performed in triplicate. Results are expressed as the total area average of bundles per cell. Images were obtained with an objective of 20X. **B.** Representative images of the assay. The pictures represent DMSO (vehicle control), LiCl 30 mM (positive control), and test compound at 10 μM and 100 μM.
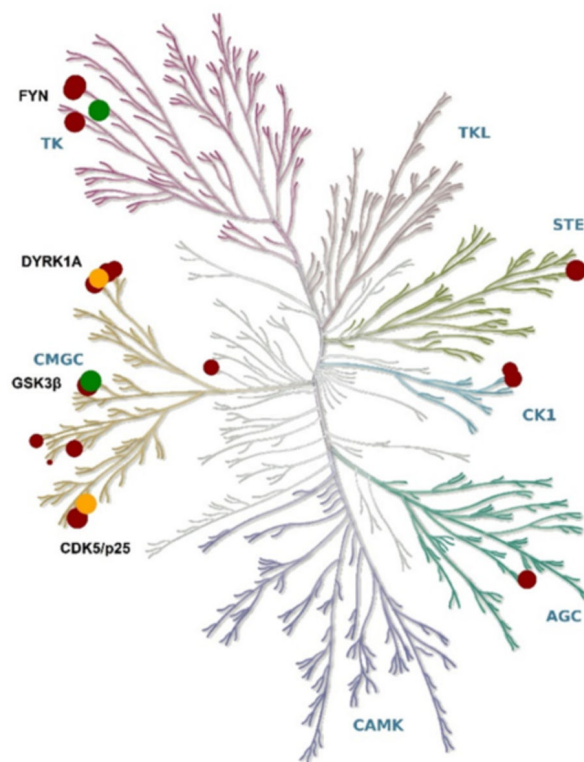
Figure 5.
Kinase tree representation of compound **4** selectivity profile toward 20 different PKs. Protein circles denote % of inhibition at 10 μM (values reported in Table 2). GSK-3β and FYN are illustrated as green circles. DYRK1A and CDK5/p25 as orange circles. All the other crossover off-target kinases, including GSK-3α, SAPK2a, MAPK1, MAP4K4, JNK1α1, PKA, cSRC, CDK1/cyclinB, Yes, Lck activated, CK1δ, DYRK1B, CK1ε, CK2, DYRK3, DYRK2 are depicted as red circles. Illustration reproduced courtesy of Cell Signaling Technology, Inc. (www.cellsignal.com).[29]
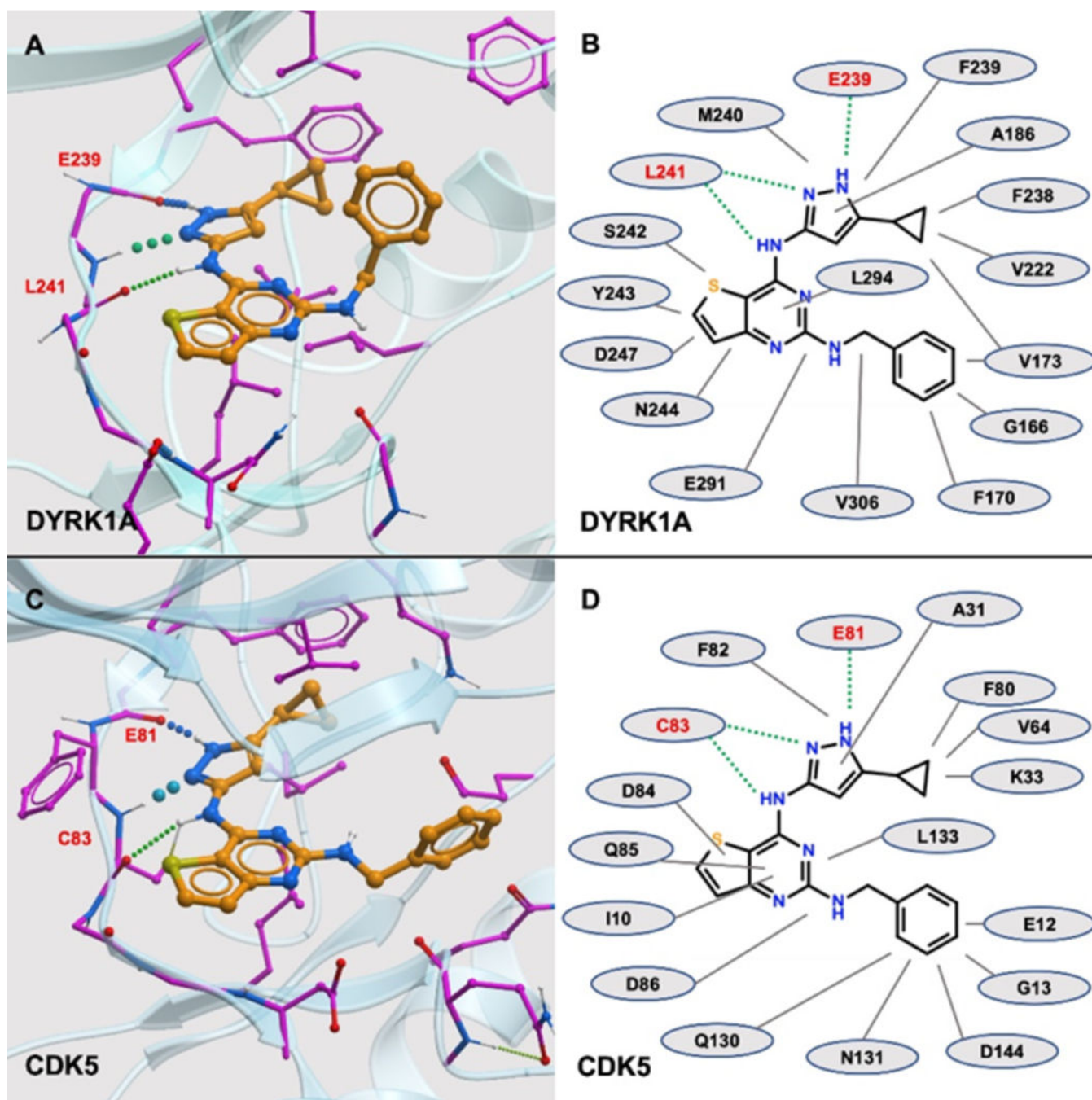
Figure 6.
Graphical representations of the binding mode of **4** to DYRK1A and CDK5. (**A**, **C**)
Structural models of DYRK1A (**A**) and CDK5 (**C**) from docking simulations. Flexible
receptor model for DYRK1A constructed from the following PDB entries: 5AIK, 4YLJ,
4YLK, 4YLL, 4YU2, 4AZE, 3ANQ, 3ANR, 4MQ1, 4MQ2, 4NCT. Flexible receptor model
for CDK5 constructed from the following PDB entries: 4AU8, 1H4L, 3O0G, 1UNG, 1UNH,
1UNL. (**B**, **D**) Schematics showing the binding pocket interactions predicted between

compound **4** and DYRK1A (**B**) and CDK5 (**D**), respectively. Dark grey lines indicate hydrophobic interactions; green dotted lines are used for hydrogen bonds.
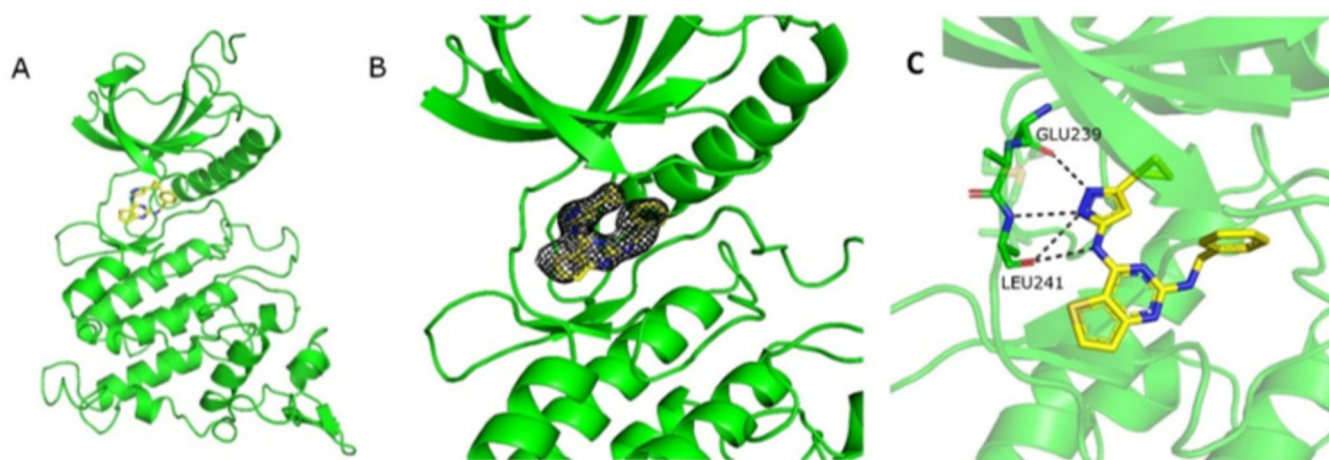
Figure 7.
Crystal structure of DYRK1A in complex with **4**. **A.** Compound **4** (yellow) in the ATP binding pocket of DYRK1A (green). **B.** Electron density map ($2F_O - FC$) corresponding to compound **4** is contoured at 1.2σ level (black mesh). **C.** Hydrogen bonding interactions (black dashes) of **4** with the backbone atoms of hinge region residues GLU239 and LEU241 of DYRK1A (green).
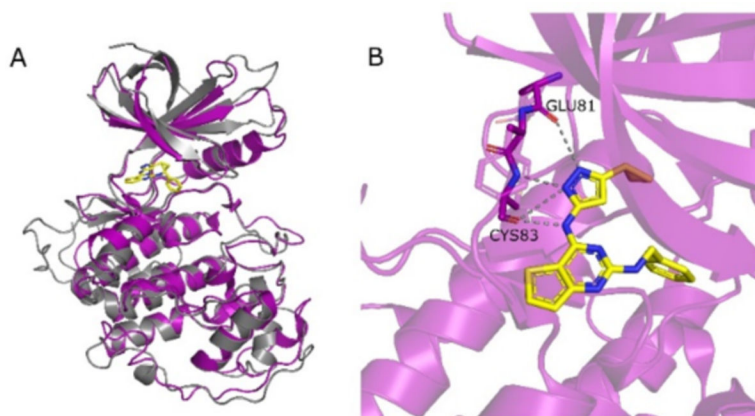
Figure 8.
Overlapping of GSK3β–**4** complex with CDK5 structure. **A.** Overlapping of CDK5 (purple) structure (PDB ID: 1UNL) with the structure of GSK-3β (grey) in complex with **4** (RMSD 1.066). Compound **4** at the ATP binding pocket of CDK5. **B.** Potential H-bond interactions (grey dashes) between **4** and CDK-5 backbone atoms (GLU81 and CYS83), based on the structures overlapping.

Table 1.

GSK-3β and FYN IC$_{50}$ values and binding affinity data of compound 4 in enzymatic radiometric and NanoBRET assays, respectively.

Cmpd ID	Enzymatic Radiometric Assay		NanoBRET Target Engagement Cellular Kinase Assay	
	IC$_{50}$ (nM)		IC$_{50}$ (nM)	
	GSK-3β[a]	FYN[a]	GSK-3β[b]	FYN[c]
	5	3	9.65	91.1
4 CHIR-99021 Dasatinib			4.78	
				2.58

[a] IC$_{50}$ values were reported as a mean value of two different determinations

[b] GSK-3β tracer K8 (0.25 μM)

[c] Fyn tracer K4 (0.33 μM).

Table 2.

Percentage (%) of inhibition of compound 4 at 0.1 and 10 μM against a panel of 20 different PKs and open targets platform-based scores.

Rank	Kinase	Kinase Inhibition %[a]		Overall Nervous System tauopathy like diseases score
		0.1 μM	10 μM	
1	DYRK1A(h)	14	92	0.89
2	CDK5/p25(h)	86	97	0.84
3	FYN(h)	100	100	0.60
4	GSK-3β(h)	94	100	0.59
5	GSK-3α(h)	96	100	0.45
6	SAPK2a(h)	13	27	0.42
7	MAPK1(h)	19	67	0.38
8	MAP4K4(h)	14	99	0.36
9	JNK1α1(h)	11	80	0.32
10	PKA(h)	9	88	0.31
11	cSRC(h)	96	96	0.30
12	CDK1/cyclinB(h)	62	99	0.16
13	Yes(h)	98	100	0.05
14	Lck(h) activated	58	97	0.04
15	CK1δ(h)	6	73	0.03
16	DYRK1B(h)	10	88	0.02
17	CK1ε(h)	0	83	0.02
18	CK2(h)	5	75	0.01
19	DYRK3(h)	19	90	0
20	DYRK2(h)	16	77	0

Kinases are ranked according to the reported overall strength of a given target–disease association from the Open target Platform (https://platform.opentargets.org) [27]. Panel of selectivity data are shown according to the following color scale: green color is associated with a high % of inhibition values; orange is associate with a modest % of inhibition; red color corresponds to a low % of inhibition.

[a] Data are reported as the mean of two independent experiments.

Table 3.

Enzymatic radiometric and NanoBRET assays data of compound 4 on DYRK1A and CDK5.

Cmpd ID	Enzymatic Radiometric Assay		NanoBRET Target Engagement Cellular Kinase Assay
	IC$_{50}$ (nM)		IC$_{50}$ (μM)
	DYRK1A^a	CDK5^a	DYRK1A^b
4 CEP701	887	40	2.09
			0.018

^{a}IC$_{50}$ values were reported as a mean value of two different measures

^{b}DYRK1A tracer K10 (1 μM).